**ORIGINAL PAPER**

# Experimental and numerical studies on small contra-rotating electrical ducted fan engines

Tobias Ebus[1] · Markus Dietz[1] · Andreas Hupfer[1]

## Abstract

Electrical propulsion has been identified as one of the key fields of future research within the aerospace sector. The Institute of Aeronautical Engineering at the Universität der Bundeswehr München aims to contribute to the ongoing development of small-sized electrical ducted fan engines with a thrust in the range of 100 N. A special emphasis is placed on electrically powered contra-rotating fan stages. When compared to a conventional rotor–stator stage, contra-rotating fan stages allow for a more compact design, considering a given pressure ratio, or an increased pressure ratio at a constant fan diameter. Since numerous new aircraft concepts are presently being developed, a high demand for compact and powerful electrically driven engines arises. Electrically driven contra-rotating fan engines provide a high potential in terms of compactness, emissions and efficiency. Using electric motors offers the ability to overcome common issues, such as design and integration of a contra-rotating stage into a gas turbine. An innovative new engine design featuring such a contra-rotating stage is developed and tested at one of the Institute's test benches for electrical propulsion. Key components are two brushless motors powering the fan stage, one for each rotor. Various operation points are investigated experimentally during an extensive test campaign. Experimental results are compared to results of numerical simulations computed by ANSYS CFX. Results indicate a good agreement between experiment and simulation. The engine is running very smooth throughout all tested operation points. Yet, intensive heating up of the electric motors and high-temperature zone are found to be an issue at higher rotation speeds.

**Keywords** Contra-rotating fan · Electric propulsion · Experimental · Numerical

## Abbreviations

| | |
|---|---|
| CFD | Computational fluid dynamics |
| CRF | Contra-rotating fan |
| DC | Direct current |
| EDF | Electrical ducted fan |
| EPR | Engine pressure ratio |
| ESC | Electronic speed controller |
| MCU | Motor control unit |
| OP | Operation point |
| PWM | Pulse-width modulation |

✉ Tobias Ebus
tobias.ebus@unibw.de

1    Institute of Aeronautical Engineering, Universität D.
     Bundeswehr München, Werner-Heisenberg-Weg 39,
     85577 Neubiberg, Germany

## 1 Introduction

During the last decades, the worldwide aerospace sector has been undergoing a remarkable development, as a variety of new business segments has been established and expanded in parallel to commercial, general and military aviation [1]. These new business segments are still evolving, including fields such as urban mobility, delivery services or surveillance missions. Numerous new aircraft concepts have been designed in accordance with their mission requirements, particularly in the field of Unmanned Aerial Vehicles and small passenger aircraft. Simultaneously, the aircraft industry is driven by the social demand to cope with ecological aspects and reduce dependency on fossil fuels [2, 3]. As a result, hybrid-electrical and full electrical propulsion systems are gaining an increasing attention within the aerospace community [4, 5]. A number of contemporary aircraft concepts already moved away from combustion engines toward electrical motors. This tendency is increasing nowadays. Currently, especially light aircraft for general aviation purposes have been equipped with electrical engines.

But, electric propulsion of larger civil aviation aircraft is an emerging sector. Brelje and Martins [6] offer a comprehensive summary featuring the most important all-electric and hybrid-electric concepts. Moreover, new aerial transportation systems require continuous improvements of propulsion systems, as well as innovative new designs, to cope with advanced mission requirements and legal regulations. Electrical ducted fan engines (EDF) are capable to meet these demands and provide potential for the future. High degrees of efficiency, as provided by the current generation of electric motors, are beneficial [7].They allow designing an EDF with a high-internal efficiency across a wide range of operating conditions. However, ducted engines in general are more advantageous at higher cruise speeds, compared to open propeller-driven engines. At moderate or low cruise speeds, propellers offer a better propulsive efficiency. Consequently, an EDF engine is particularly suitable for applications with higher flight speed. Besides these abilities, a conceptual ducted engine powered from electric motors additionally offers important advantages. Engines with shrouded rotors may be integrated into an aircraft fuselage more easily. This enables airframers to move the engine to a more advantageous position. Moreover, electric engines can be designed in a more compact way, saving space and weight. An electric engine does not feature any hot parts that may threaten the airframe structure and require supplemental coating or housing. Hence, additional savings of structural weight can be achieved. Shrouded engines also benefit from their casing with respect to noise emissions, compared to unducted propellers. The casing attenuates large amounts of the noise caused by the rotating components. Integrating an engine into the airframe enhances this effect. Finally, ducted engines provide a high specific thrust relating to the cross-sectional area. In summary, future research on ducted electric fan engines should focus on improving both internal and propulsive efficiency to allow these engines to compete against propeller-driven engines in the low-to-moderate cruise speed segment. At this point, the contra-rotating fan engine (CRF) is unfolding its potential to achieve the abovementioned goals and become a game changer. Figure 1 depicts an exemplary model of a CRF. Strictly speaking, conceptual contra-rotating fans have already been introduced during the last century, being integrated in gas turbine engines. Anyway, integrating and synchronizing contra-rotating fans into an engine powered by a gas generator is both complex and expensive—a common drawback all these concepts suffered from. Most of the conceptual engines never attained more than prototype status [8]. Due to the ongoing enhancement of electric motors, a new opportunity arises to implement contra-rotating fan stages into aircraft engines, successfully.

This paper addresses advantages and drawbacks of contra-rotating fans, their design in general and in particular,
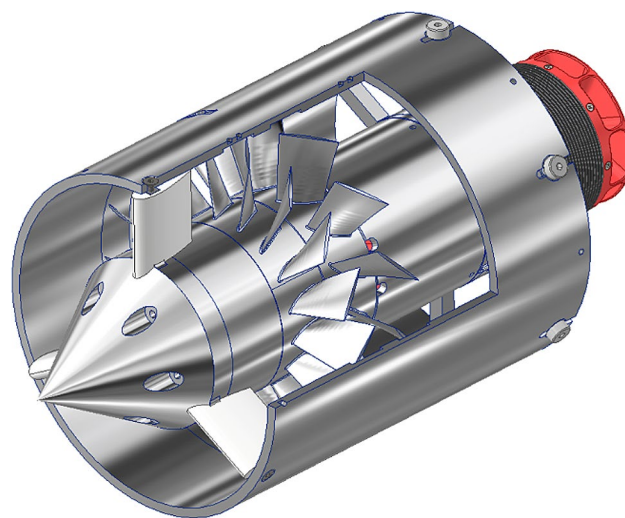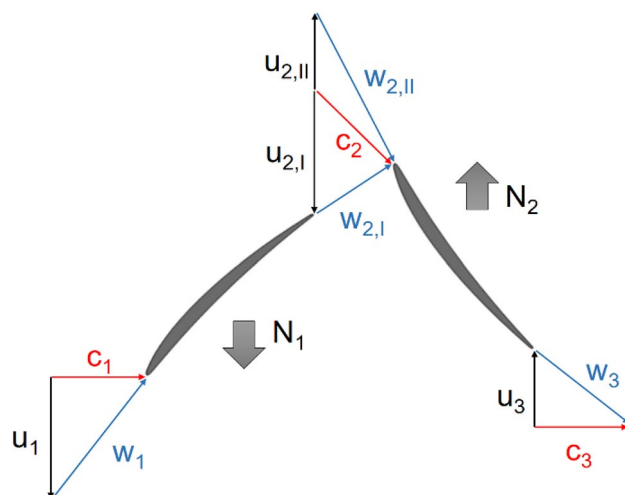
**Fig. 1** Contra-rotating fan engine



**Fig. 2** Velocity diagram of a CRF

considering the CRF owned by the Institute. An additional description of the test bench will be offered, together with an introduction to the utilized measurement techniques. Finally, this study will feature a set of experimental data from measurements and will attempt to compare these with numerical results from simulations with ANSYS CFX.

## 2 Contra-rotating fan

### 2.1 Basic principle

Unlike any conventional rotor–stator stage integrated into contemporary turbo compressors or fans, a contra-rotating stage features two rotors with opposite direction of rotation

and no stator in-between. Figure 2 exhibits the rotor–rotor configuration with its corresponding velocity diagram at the meridional cross-section. Both blade rows rotate with their rotational speed N, which induces a circumferential velocity component u in direction of rotation. Since the velocity diagram is considered at a constant radial position, the velocities $u_1$ and $u_{2,I}$ are assumed equal, as well as the velocities $u_{2,II}$ and $u_3$. Moreover, c denotes the absolute velocity and w denotes the relative velocity each blade row encounters. When monitoring the velocity diagram carefully, it becomes apparent that the swirl introduced by the front rotor is removed from the flow by the rear rotor together with a simultaneous energy input. Thus, a contra-rotating stage at an ideal operation condition provides a nearly swirl-free exit flow, analog to a conventional rotor–stator stage, without the need of a stator. Stators usually are utilized to increase the static pressure level of a flow without power input, by diminishing the swirl and consequently reducing its kinetic energy. A loss of total pressure is inevitable for stators, as there is no power supplied to the flow and the flow itself suffers from losses, e.g. due to friction. However, a contra-rotating stage has two rotors, which gain mechanical power from a shaft and both of them contribute to the total pressure rise. Accordingly, the swirl of the flow is reduced while in parallel the total pressure is increased.

Distributing the total pressure rise onto two rotors rather than one, offers potential to reduce the load on the front rotor, resulting in a better overall stage efficiency. Various researchers have already addressed this effect in numerical and experimental studies [9–11]. Moreover, contra-rotating stages have been found to provide a good off-design performance over a wide range of operation points [12]. Therefore, it appears to be reasonable to optimize contra-rotating fans, with respect to overall efficiency, by finding the best possible distribution of load. Alternatively, another justified approach may be taken by increasing the overall total pressure rise capability of the stage. As a result, a higher specific momentum is available at the exit of the stage. The maximum cruise velocity of an aircraft is determined by the level of this specific exit momentum and the way it is converted into velocity in a downstream nozzle. Consequently, a fan pressure ratio enables an engine to achieve higher cruise velocities.

## 2.2 Design aspects

Due to the coaxial rotors with opposite sense of rotation, a contra-rotating stage features a more complex design compared to a conventional stage. In principle, we may find two distinct technical solutions to overcome the problems related to coaxiality within a stage:

- Using a single power source, e.g. a turbine stage or a motor, to drive both rotors simultaneously.
- Using separated power sources, e.g. two turbine stages or motors with opposite direction of rotation, to drive both rotors independently.

The first solution necessitates a gearbox to initiate the contra-rotating movement of the two rotors. Installing a gearbox comes along with a lot of additional weight and complexity, both absolutely undesired in engine design. An additional drawback of a gearbox is a limited ability to vary the rotation speed ratio. Unlike the first concept, the second technical solution provides two separate power sources, such as two electric motors, which may be operated independently. Independent power sources allow for a flexible variation of the rotation speed ratio, giving an additional degree of freedom when designing or operating such a system.

Aerodynamic design of both rotors is one major aspect, which has to be taken into consideration when designing a contra-rotating system. As designer, you have to determine how to distribute the total aerodynamic load onto your two rotors. With this parameter fixed, rotation speeds, blade angles and velocity diagrams can be found. It is important to mention, that the rear rotor has to be designed in accordance with the swirl angle from the front rotor's exit. Previous studies have revealed a distinct influence of the axial gap between front and rear rotor, as the size of the gap directly affects the overall efficiency of the system [13]. Large-sized gaps enable perturbations and turbulences to attenuate over a longer distance, reducing their impact on downstream blade rows. Small-sized axial gaps facilitate interaction between two adjacent blade rows and enhance losses due to wakes and potential effects. On the contrary, longer axial distances between two blade rows support diffusive and convective processes, which in turn diminish the swirl and thus involve a loss of kinetic energy. As a result, downstream blade row leading edges are prone to higher incidence angles and corresponding losses. Up to the present, there are no generally applicable design guidelines available dealing with the sizing of axial gaps in contra-rotating stages and each design has to be examined separately. A meaningful approach to increase overall efficiency is systematically varying the axial gap of a validated baseline concept in additional experiments or simulations.

Comparing a small ducted contra-rotating engine with a net thrust of approx. 100 N to a large-sized civil aviation turbofan of conventional architecture with a thrust in the range of a few hundred kilonewton, reveals a distinctive three-dimensional flow behavior, largely influenced by friction and accompanied by secondary flows. These three-dimensional flow structures are advantaged by a larger fraction of low-energized fluid in wall-near boundary layers, as well as by lower relative blade heights and larger relative

blade tip gaps. Simply downscaling a larger engine will not do the job when designing a small-sized axial fan. Designers have to identify all relevant flow features in a small fan that need to be considered during design, especially those characteristic for contra-rotating systems. Each aspect has to be similarly addressed to estimate its impact on design and operation. Eventually, a good compromise between all relevant aspects has to be found.

A special emphasis has to be laid on profile losses due to low Reynolds number flow separation. These so-called laminar separation bubbles occur at low or moderate Reynolds number at or below $Re \leq 2 \cdot 10^5$. This study features a small-sized fan with moderate inflow velocity and small blade chord lengths. We believe the Reynolds number is very likely to be within the prone range, especially considering the upstream front rotor. Thus, flow separation and reattachment on the suction side of the blades may be an issue during distinctive operation conditions. The rear rotor is assumed to remain free from such laminar flow separation issues, as it encounters higher relative flow velocities and turbulence, caused by the swirl of the front rotor.

## 2.3 Contra-rotating test engine

A test engine has been developed and built at the Institute of Aeronautical Engineering to allow for extensive investigation of the flow behavior inside a small-sized contra-rotating engine. Figure 3 shows the engine with equipped speed controllers and sensing devices.

At this point, we will only present a short summary of relevant design parameters and the basic constructional implementation of the concept into a functional engine. A full description of the detailed design process can be found in Ebus and Di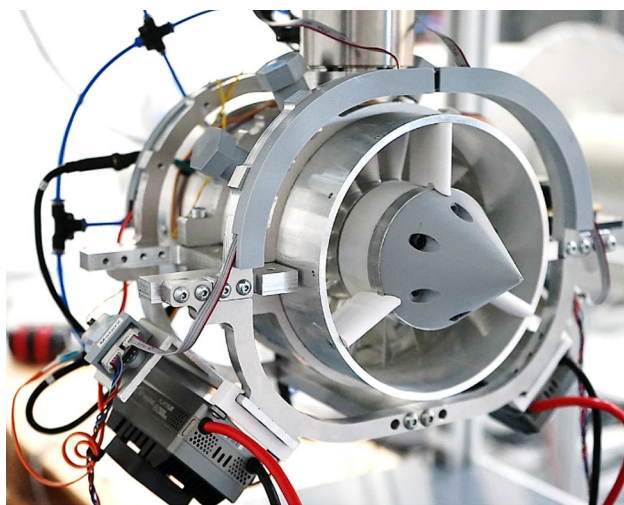etz [14]. The test engine was designed using a customized in-house tool, which is based on a streamline curvature approach to account for the axial gap between the rotors. Basic intention was to provide a test engine for a broad range of aerodynamic measurements, focusing on secondary flows and the swirl behavior in the axial gap between the two adjacent rotors. Thus, the engine was designed to deliver a maximum thrust of 100 N at an air mass flow of 1.35 kg/s. The annulus between hub ($D_H = 70$ mm) and casing ($D_C = 132$ mm) consists of a total area of 9,830 mm$^2$. Both rotors within the contra-rotating stage feature blade profiles from NACA-65 family. The front rotor is equipped with 17 blades, each with a hub chord of 16 mm and a tip chord of 25.4 mm, while the rear rotor has 13 blades which feature a hub chord of 18.8 mm and a tip chord of 23.3 mm. Uneven prime numbers have been chosen for the blades to reduce interference frequencies. Both rotors may be replaced by others to study in how far a variation of blade parameters, such as profile type or camber influence strength and effect of losses. To enable easy exchanging, the rotors are individually mounted onto their corresponding shafts. Two brushless direct current (DC) motors are taken to provide power to the rotors. Both DC motors are capable of providing a shaft power of 5 kW at rotation speeds up to 25,000 rpm. Each rotor is driven by its individual brushless DC motor. Since the motors have an outer diameter of 62 mm, they may easily be integrated within the hub of the engine. Both DC motors are aligned in axial direction with coaxial output shafts. Note, that in the current configuration, the front motor is used to power the rear rotor, while the rearward motor drives the front rotor. This is a characteristic feature and will be explained in the following paragraph and based on Fig. 4, which shows the basic bearing concept of the engine. The central power shaft is supported by both, the front and rear strut, and is connected to the rotating part of the backward brushless motor via press fit. A pressure spring within the nose cone is used to prevent the bearings from axially moving inside their fittings.

The stationary parts of both DC motors are back-to-back mounted to the rear strut and therefor connected to the
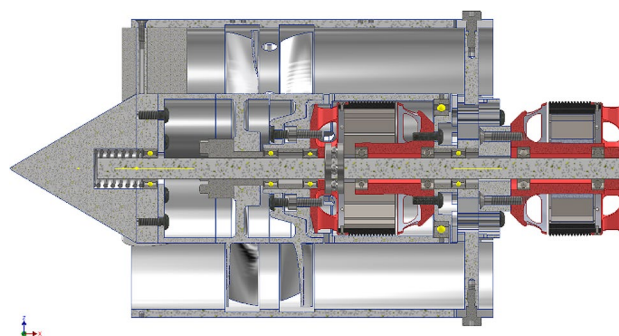


**Fig. 3** CRF developed by the Institute with equipment



**Fig. 4** Conceptual mechanical design, including bearings

casing. Both have internal bearings to support the central power shaft. Since the rear brushless motor drives the front rotor via central shaft, the rotor is fixed to the shaft with a mounting set. Unlike the front rotor, the rear rotor is directly mounted to the rotating part of the front brushless motor without an additional shaft. It is equipped with two additional bearings, one at the front end, supporting the central shaft and the other at the rear end, taking support from the rear strut. Choosing this configuration with two bearings reduces the risk of the rotor banking out when powered. Bearings between central shaft and front motor must be able to accommodate the highest possible rotation speeds due to the opposite rotation directions. We assume these bearings to be the first to suffer from deterioration. Consequently, the conceptual design offers an opportunity for these bearings to be replaced, easily.

The front rotor is designed to run 25,000 rpm at full speed with the rear rotor operating at a slightly lower rotation speed of 21,250 rpm. Thus, a resulting rotation speed ratio of 0.85 is attainable at design conditions. This equals the distribution of power and load between the two rotors of the stage. A moderate total pressure ratio of 1.085 has been chosen, since approving the mechanical concept and providing a test model for further studies were the main goals of this study, rather than optimizing the pressure ratio. Table 1 summarizes important design parameters of the engine.

Casing, struts and both rotors are manufactured from aluminum alloy. To prevent the rotor tips from rubbing the inner casing, two circumferential grooves have been manufactured inside of the casing, giving some additional 1.5 mm of tip clearance to the blades. Without these grooves, the tip gap size would be 0.5 mm in absence of any thermal or mechanical loads on the blades. As blades will both, lengthen and bend due to static and dynamic loads during operation, increasing the tip gap size appears to be a reasonable countermeasure to avoid damage.

As mentioned earlier, the front rotor is fully integrated within the hub of the engine and requires venting slots to

**Table 1** Important design parameters

| Quantity | Symbol | Unit |
| --- | --- | --- |
| Thrust | F | 100 N |
| Power consumption | P | 10 kW |
| Supply voltage | U | 52 V |
| Mass flow | ṁ | 1.35 kg/s |
| Total pressure ratio | π | 1.085 |
| Rotation speed R1 | N1 | 25,000 rpm |
| Rotation speed R2 | N2 | 21,250 rpm |
| Rotation speed ratio | ξ | 0.85 |
| Blade number R1 | B1 | 17 |
| Blade number R2 | B2 | 13 |

dissipate its internal heat away, preventing the motor from overheating. These ventilation slots are positioned behind the rear rotor and are designed to allow some venting air to flow through the hub and cool down the motor.

Each motor is controlled by an individual Electronic Speed Controller (ESC) via pulse-width-modulated (PWM) signals. Both ESCs are slave devices to a master motor control unit (MCU), consisting of a micro controller with a customized configuration.

## 3 Experimental investigation

To generate a good understanding of the engine operating under different conditions, a series of experiments have been conducted as ground tests for non-flight conditions. These are hereafter referred to as static tests. Relevant parameters have been measured and recorded to allow for a detailed evaluation:

- Thrust F
- Mass flow ṁ
- Static pressure p
- Electric power consumption $P_{el}$ for each motor
- Rotation speed of both rotors N1 and N2

Electrical resistance and mechanical losses within the entire system, which moreover depend on actual operation conditions, deteriorate available shaft power for both the rotors. Hence, the electric power consumption gives a good indication of the overall shaft power required by the stage, rather than exactly quantifying the amount necessary to drive the rotors.

A standard inlet, in accordance with standard ISO 5801 [15], is used to determine the air mass flow through the engine. The ISO standard defines relevant design aspects, which have been considered during construction phase, as well as guidelines for taking measurements and post-processing results.

Measured quantities are not only used to check the engine's behavior, but are also taken as input parameters for numerical studies with ANSYS CFX, defining relevant boundary conditions. For this purpose, static pressure is measured across both, inlet and outlet stations of the engine. Figure 5 indicates these inlet and outlet stations and provides some additional information about their axial position.

In addition to the two aforementioned static pressures, the total pressure across the inlet is an important boundary condition for numerical investigations.

To complete the set of boundary conditions, environmental pressure and temperature are measured. Since there is no
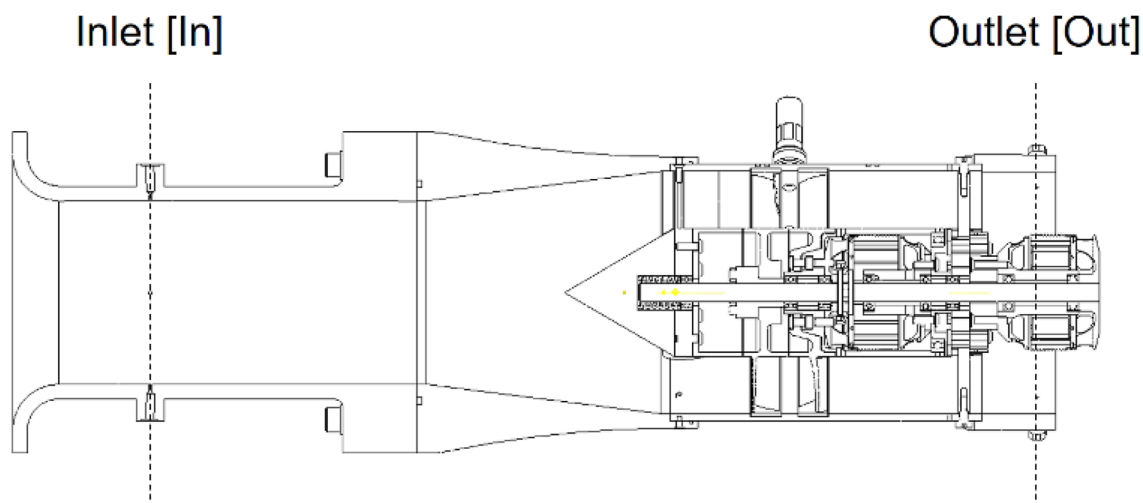
**Fig. 5** Inlet and outlet stations for measurement

inflow velocity, these static conditions are afterwards taken as the reference stagnation conditions for CFD simulations.

### 3.1 Test bench

The test bench, which has been utilized for performance measurements, is depicted in Fig. 6. Its main modules may be grouped as follows:

- A mobile rack supporting the power supply unit for powering the motors
- A support structure with a multi-axis combined force and torque sensor to which the engine is mounted
- The fully equipped engine with all its controllers, sensors and telemetry devices

Power is supplied by a 15 kW direct current power supply unit, which is capable of voltages up to 60 V. Due to its high output, the unit is able to simultaneously supply power to both motors. Both ESCs are directly powered by the supply. For this reason, they are mounted below the engine, one on each side. This allows optimal access to the ESC wiring on both ends. For the sake of simplicity, the complete engine with all its supplementary equipment is mounted to the force and torque sensor. As mentioned earlier, the engine is equipped with two ESCs (one for each rotor), the MCU of the engine, telemetry systems transmitting relevant motor data, various pressure sensors and the flange-mounted standard inlet. The fully equipped engine is shown in Fig. 7.

### 3.2 Measurement instrumentation

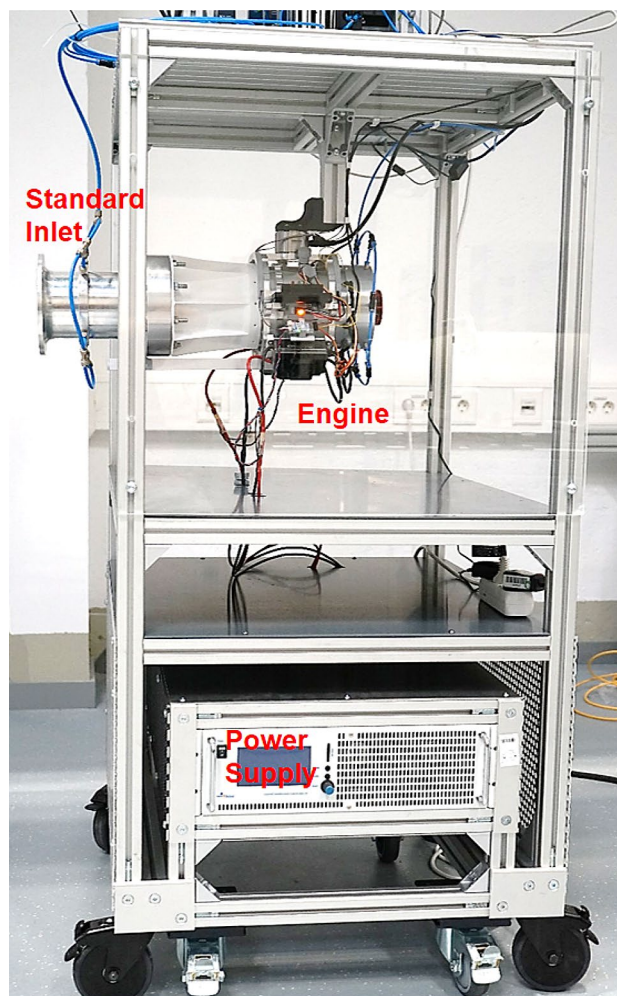As a variety of different parameters has to be observed during testing, a number of unique sensing techniques
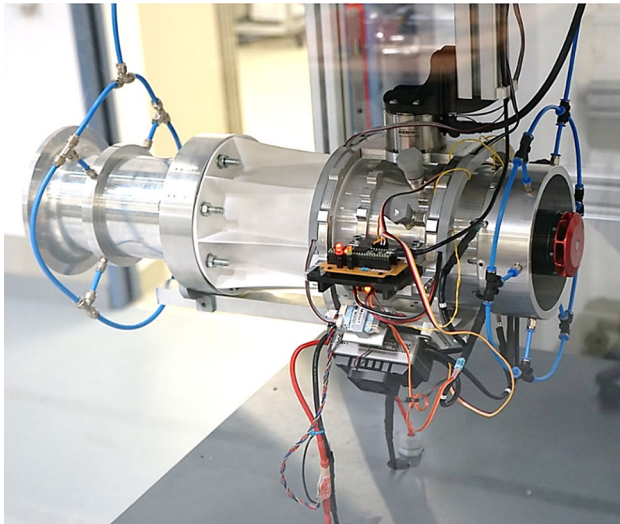


**Fig. 6** Test bench for CRF

**Fig. 7** Fully equipped engine

is utilized. Data gathered by these techniques are collected by a measurement software written in LabVIEW for special use with this engine test bench. The present experimental investigation focuses on stationary testing of the engine under different operation conditions. Consequently, a rather moderate frequency of 10 Hz is selected for continuously acquiring data from sensors.

### 3.2.1 Thrust

To gain information about the thrust produced by the engine, a 6-axis combined force and torque sensor is used. This type of sensor is capable to capture all applied forces and moments to a point of reference. For this purpose, the sensor consists of six combined Wheatstone bridges. When loads are applied, the sensor displays a one-dimensional signal vector composed from six signals, each from one of the Wheatstone bridges. Post-processing is required to calculate the resulting load vector from this signal vector by multiplying a matrix with constant elements, which is unique for each sensor. The system as presented in this section is capable of measuring forces up to a maximum value of 500 N and torque up to 20 Nm. It allows repeating any measurement with an accuracy of 0.2% of the maximum value. Measuring the thrust force of the engine is feasible with an accuracy of $\pm 1$ N for the chosen sensor configuration and installation.

Prior to any measurement campaign, our sensor is calibrated with an accuracy of 0.1 N to compensate for any

offset. These offset values are submitted to our measurement software where an automated correction of incoming force and torque values is performed.

### 3.2.2 Pressure

Static and total pressure values are obtained using digital piezo-resistive sensors with 14 bits of resolution. Multiple sensors are aligned to a microcontroller in charge of collecting the data, calculating the corresponding physical value, bundling these values and sending them to the measurement software. A standard serial protocol is used for transmitting data. We use absolute pressure sensors with a range of 0–1.6 bar combined with differential sensors, which feature an effective range of 400 mbar. In terms of accuracy, we conclude that we are able to measure an absolute pressure accurate to approx. 10 Pa when using a 14 bit-resolution sensor. Differential sensors may even output their signal with an accuracy as good as five Pascal when operating at 14 bit. According to the related data sheet, each sensor is expected to provide a maximum offset of 1%. During preparation process, each pressure sensor is calibrated for its relevant effective range using a pressure calibrator. Again, these offset values are recorded and submitted to our measurement software. Our results of the calibration procedure confirm there indeed is a constant offset for each sensor, but always within the tolerated range according to the specifications.

Measuring static pressures is relevant for the inlet and outlet stations according to Fig. 5. At the corresponding axial stations, there is a number of circumferentially uniformly distributed pressure holes. Inlet pressure is taken by four holes, outlet pressure by six holes. For both stations, static pressure is physically averaged across all circumferential holes by a circular pneumatic tube. As we mentioned earlier, there is no need for an exact time-resolved pressure signal and thus we extend the pneumatic tubes between pressure hole and sensor to a few meters of length. By this means, the tubing physically damps pressure fluctuations from disturbances or similar and we receive a more smooth signal readout.

### 3.2.3 Rotation speed and power

An off-the-shelf telemetry system for brushless motors is used to transmit speed and power information from both our motors. The system utilizes a high-precision resistor to measure the current rating inside the live wire between power supply and ESC. The current is not directly measured, but calculated from the voltage drop across the resistor. In addition, the voltage between live wire and ground is measured for the input lead and the power consumption of a single motor is calculated as current times voltage. Moreover,

**Table 2** Operation points being considered

| Operation point | N1 [rpm] | N2 [rpm] | ξ [-] |
|---|---|---|---|
| OP1 | 1,883 | 1,660 | 0.88 |
| OP2 | 6,042 | 5,238 | 0.87 |
| OP3 | 10,630 | 9,080 | 0.85 |
| OP4 | 15,400 | 12,820 | 0.83 |
| OP5 | 19,580 | 16,355 | 0.84 |

the telemetry system is able to sense rotation speeds by measuring the frequency of the commutated output signal of the ESC. The user has to provide information about the number of pole pairs and the telemetry calculates the rotation speed. All values are bundled and transmitted to the measurement software via serial connection.

### 3.3 Procedure

Measurements are performed at constant operation conditions. Transient processes are not within the interest of this study and therefore are not examined. As can be seen from Table 2, each pair of rotation speeds defines one specific operation point (OP) with a distinct mass flow and thrust.

At this point is appears to be worth mentioning, that our actual configuration did not allow for an investigation of operation conditions above 20,000 rpm, as the motors tended to heat up rapidly when approaching this threshold. A redesign with an integrated cooling concept is required to widen the rotation speed margin. Within the scope of this study, we therefore do not consider rotation speeds above the mentioned threshold during our experimental test campaign and focus on the speeds given in Table 2. All listed operation points were approached precisely and maintained constant during measurement. Measurements are performed after the desired operation point has been approached and engine operation remains steady. For a period of 10 seconds, measurements are performed and the data are processed to the software. The corresponding values for each OP are afterwards mathematically averaged and the standard deviation is calculated, as explained in the next section.

### 3.4 Results

We have conducted a series of tests with our novel contra-rotating engine to study its performance and behavior. This chapter deals with our collected experimental data, their analysis and the corresponding results. For the sake of clarity, we present all relevant parameters as a function of the mass flow, where we will highlight our operation points. Usually we would correct the mass flow with regard to known reference conditions, but as we conducted all experiments at equal environmental conditions, we will dispense

correcting our results. Environmental conditions, such as temperature and pressure were measured and recorded during tests. Due to the short test phases, all conditions were found to remain constant.

To begin, the chart displayed in Fig. 8 illustrates both rotation speeds as a function of our mass flow. By closely examining this chart, we may directly identify a quasi-linear correlation between these two parameters—just as we might have expected. The identified correlation is based on the mass flow being proportional to the absolute component of the axial velocity, as stated by the continuity equation. From the velocity diagram in Fig. 2 we conclude, that our absolute axial velocity in turn is directly proportional to the circumferential velocity and hence the rotation speed. For any incompressible flow through a contra-rotating stage, we will find that varying the rotation speeds will scale all vectors inside our velocity diagram in an equal manner, if the ratio of rotational speeds remains constant.

The present case is characterized by moderate flow velocities below the commonly accepted threshold of Mach 0.3. Therefore, the flow may be considered as incompressible and the mass flow increases linearly with the rotational speed. From the results in Table 2, we additionally deduce, that the second constraint of a constant rotational speed ratio is met. The results are similar for all tested operation points, with only little discrepancy. For the sake of completeness, Fig. 8 does not only show the arithmetically averaged values associated with individual operation points, but also provides information about the
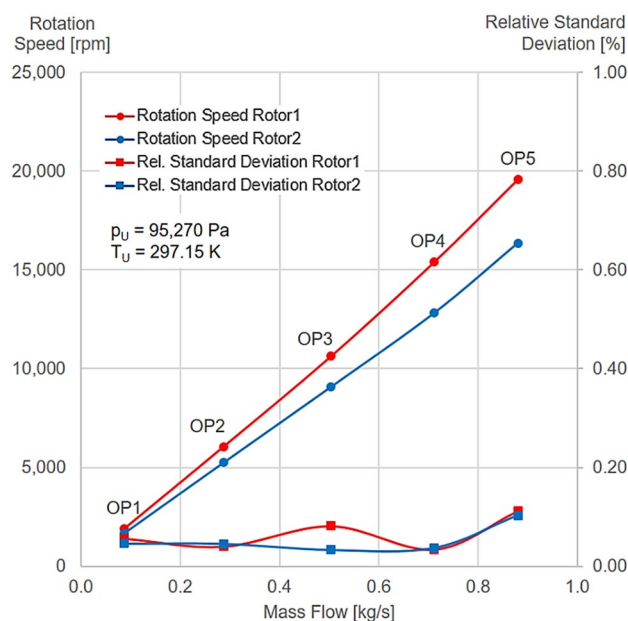


**Fig. 8** Rotation speeds as a function of mass flow, including relative standard deviation

relative standard deviation calculated among all measured values. Values for the given empirical standard deviation are calculated using the following equation:

$$s_{rel} = \frac{s}{\bar{x}} = \frac{1}{\bar{x}} \cdot \sqrt{\frac{1}{n-1} \sum_{i=1}^{n} \left(x_i - \bar{x}\right)^2} \tag{1}$$

With $s$ representing the standard deviation, $x_i$ representing the actual value (from 1 to $n$) and $\bar{x}$ representing the averaged value. Remembering the standard deviation values from Fig. 8 we realize, our sensors measuring the rotational speed provide good and accurate measurements with an error in the magnitude of 0.1% of the maximum value. We consider this sufficient.

Figure 9 presents a plot highlighting the engine's net thrust as a function of mass flow. A nearly quadratic trend of the thrust may be observed for increasing mass flow, just as the momentum equation implies:

$$F = \dot{m} \cdot \left(c_9 - c_0\right) = \dot{m}^2 \cdot \left(\frac{1}{\rho_9 \cdot A_9} - \frac{1}{\rho_0 \cdot A_0}\right) \tag{2}$$

Density $\rho$ and area $A$ are additional factors affecting the thrust, although the quadratic mass flow generates a larger impact. Since our experiments have been conducted as static tests with zero inflow velocity, the second term within the brackets may be neglected. At a rotational speed of approx. 19,500 rpm, the thrust is maximized to 75 N. This is operation point OP5. Again, the relative standard deviation values are estimated according to (1). Among all considered operation points, relative standard deviation values are found not to exceed 0.5%, except for OP2. We are therefore encouraged, that our force and torque sensor is able to generate precise and reliable data for its entire range.
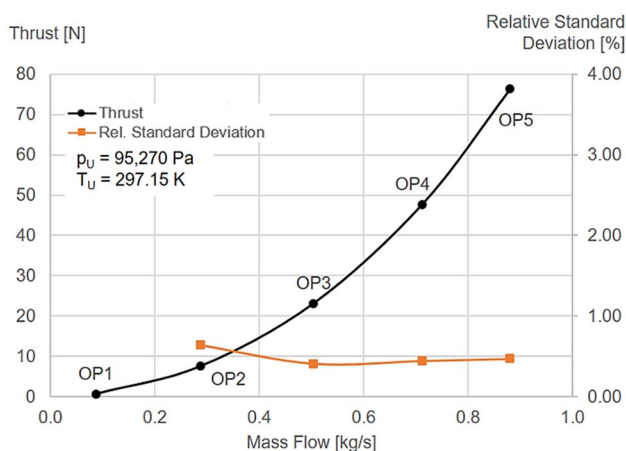


**Fig. 9** Thrust as a function of the mass flow, including relative standard deviation
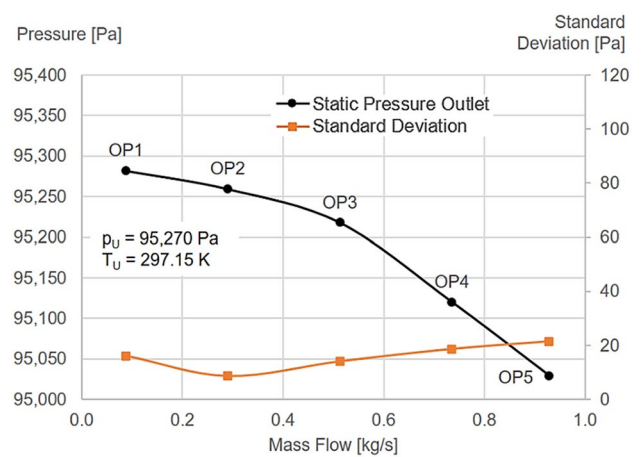


**Fig. 10** Static outlet pressure as a function of mass flow, including standard deviation

Finally, we would like to check upon static pressure values measured at our outflow station. Corresponding values are illustrated in Fig. 10, again as a function of the mass flow. The plot indicates a strong dependency between back-pressure and mass flow. An increasing mass flow forces the static pressure in our outlet to decline. This phenomenon appears to be logic as so far, as an increasing mass flow results in larger flow velocities at the outlet station of the engine. Thus, a larger shear layer gradient develops between exiting and surrounding flow. The surrounding flow becomes accelerated from zero velocity in the presence of this shear layer and a local drop in static pressure originates. We assume that this pressure drop can still be detected inside the duct at our outlet measurement station.

For all considered operation points, the pressure drops below environmental conditions. Higher exit velocities result in a larger pressure drop. To complete, Fig. 10 provides information about the standard deviation values for the given pressure measurements. Values between 10 and 20 Pa are apparent, which is well within the measurement accuracy for absolute pressure sensors, as described in Sect. 3. We infer from these results, that our pressure sensors provide stable signals with minimal fluctuation.

## 4 Numerical investigation

Numerical studies are performed in parallel to simulate experimental operation points. Simulations are executed using ANSYS CFX to validate the chosen methods and obtain a valid numerical model for future investigations. Realizing a trade-off between numerical model complexity and computational effort is common practice—an approach we share throughout our simulation process. The simulation process will be outlined in the following paragraph.

To begin with, both rotors have blade counts, which are uneven and prime numbers, making the largest common divisor be one. Although this is highly favorable in terms of aerodynamics and aeroacoustics, certain problems arise when approaching such a system with numerical methods. Since there is no larger common divisor other than one, the domain cannot be divided into periodic sectors to save computational time. Consequently, an entire engine with all blade passages in 360° has to be taken into account during simulation to capture all effects, exactly. Such an approach may be time-consuming and thus undesirable when simulating more than one operation point. To avoid large computational times and save resources, OP5 is fully simulated, at first instance. Afterwards, the domain is split into several single blade passages and one of these passages is simulated. Results between full simulation and passage simulation are then compared. A single blade passage is assembled from one blade passage from each rotor and one passage from both the front and rear strut. As these passages do not geometrically match at their interfaces, information being exchanged across the interface may be circumferentially distorted to a certain extend. From now on, this geometric mismatch is referred to as pitch angle. This study takes advantage of a mixing plane approach to model interfaces between adjacent domains. According to ANSYS, this approach utilizes a technique to submit circumferentially averaged data between two adjacent domains. Moderate pitch angles are assumed uncritical [16]. Comparing full simulation and single blade passage results, for example, by considering static pressure values, reveals only small discrepancies. Therefore, possibly distorted results appear to be negligible and remaining operation points are investigated by simulating a single passage, as depicted in Fig. 11. The details are discussed in the following section.

### 4.1 Setup

As a start, Fig. 11 intends to provide an overview of a blade passage domain, consisting of four axially aligned sub domains. The flow enters the domain through the interface marked as "Inlet", which is identical to the inlet station as
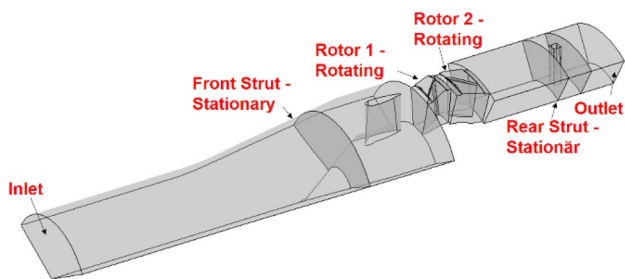


**Fig. 11** Entire domain for numerical simulation

defined in Fig. 5. The same applies to the outlet station, where the fluid exits the entire domain. Boundary layers are geometrically resolved using prism layers. Turbulence is mathematically modeled by applying the sst-model. To simplify the numeric setup, turbulent inflow conditions are selected. Hence, possible laminar separation bubbles cannot be modeled. However, these are not within the primary focus of this study. For the inlet boundary, total pressure and total temperature are prescribed, based on environmental conditions during experiments. These are taken as reference conditions and thus are equal for all numerical simulations. Static pressure is chosen as outflow boundary condition—these values were measured at the outlet station of the engine during experiments.

Flow field calculations were carried out by solving the Reynolds-averaged Navier Stokes Equations in combination with the aforementioned turbulence model. Simulations started with two defined abort criteria. Primary criterion is the simulation converging. Convergence is checked by monitoring the mass flow across the inlet section. As soon as variation of the mass flow between two iteration steps reduces to a magnitude below 0.1%, the solution is accepted converged. Root mean square (RMS) values of residua for all conservation quantities are of the order $10^{-5}$ or $10^{-6}$. Secondary abort criterion is an iteration step count of 2,000 or above, which never happened. For numerical simulations, it is common practice to provide a grid study, to ensure all results are independent from the chosen mesh. This study incorporates three different meshes with varying numbers of nodes and elements. These are hereafter referred to as:

- Baseline mesh (approx. 4.4 m. nodes)
- Low-density mesh (nodes reduced by 20%)
- High-density mesh (nodes increased by 20%)

A single blade passage at OP5 is calculated for each mesh. Mass flow and total pressure rise of the entire engine are compared to gather information about the mesh dependency. Results are summarized in Table 3. All three meshes appear to provide similar mass flows and total pressure rises. Mass flow results vary by no more than 1%, which is within the experimental measurement accuracy of a standard inlet as proclaimed by ISO 5801. According to these findings, we assume the mesh induces no additional distortion, when

**Table 3** Grid dependency study

|                        | Low density | Baseline    | High density |
| ---------------------- | ----------- | ----------- | ------------ |
| Nodes                  | 3.593.000   | 4.410.000   | 5.238.745    |
| Elements               | 3.437.000   | 4.241.000   | 5.036.606    |
| Pressure rise (Total)  | 4391 Pa     | 4421 Pa     | 4278 Pa      |
| Mass flow              | 0,966 kg/s  | 0,956 kg/s  | 0,954 kg/s   |

**Table 4** Results OP5 for full annulus and single passage

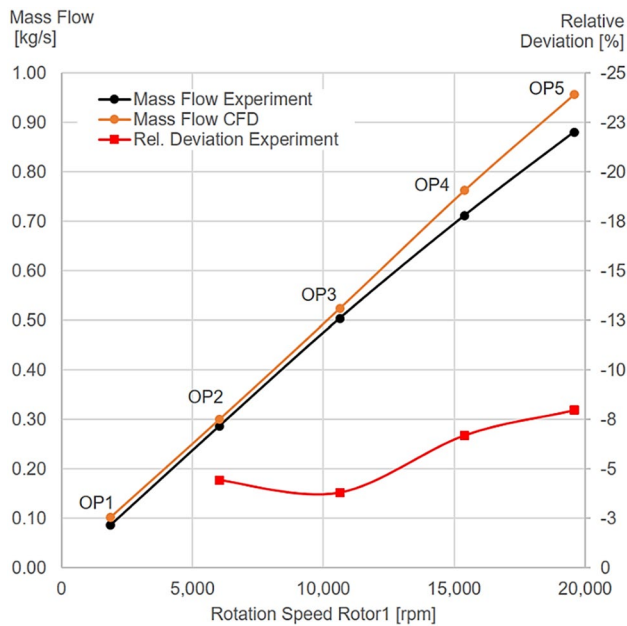| Parameter | Full annulus | Single passage |
|---|---|---|
| Mass flow [kg/s] | 0,967 | 0,956 (−1,1%) |



**Fig. 12** Comparison of mass flows between experiment and CFD simulation

comparing numerical and experimental results. The baseline mesh is selected as a good compromise between accuracy and computational effort.

## 4.2 Results

To begin, results from a full annulus simulation of OP5 are compared to those gathered from simulating a single passage. Table 4 shows calculated mass flows from both numerical simulations, including percentaged deviation. Mass flow between both simulations deviates by approx. 1.1%. Again, this is within the accuracy we would expect during measurements with a standard inlet. Hence, it is assumed sufficient. Full annulus simulations may be reproduced by single passage simulations without losing noteworthy accuracy due to distortion effects.

Fully converged numerical solutions were obtained for all considered operation points, except for OP1. For this reason, OP1 is excluded from the following analysis and only OP2 to OP4 are taken into account. Figure 12 displays the mass flow as a function of the front rotor's (Rotor1) rotation speed. To allow comparing numerical and experimental results, the mass flow from Fig. 8, representing experimental data, is also plotted in this figure. Both data

rows show a distinct, nearly linearly trend toward higher rotation speeds. However, the mass flow from experimental data appears to be less in all plotted operation points, compared to its numerical counterpart. In reality, higher losses induce a larger decrease of total pressure. When sustaining larger losses in total pressure, the engine tends to run throttled to a small extent, thus reducing the mass flow. Total pressure losses may be caused by the following mechanisms:

- Losses due to motor wiring inside the channel. These connect the brushless motors inside the hub with the power supply outside the engine. During model generation, they were not taken into account
- Thickening of the inlet boundary layer. During pre-processing, this was not taken into account
- Gaps, e.g. between stationary and rotating parts. Not all of them were considered during modeling

An additional aspect is heat transfer into the flow by the two brushless motors inside the hub. Heat transfer from inside the hub forces local temperature to increase and local density to decrease. Physical response of the flow may be a local increase of velocity to meet continuity or a globally reduced mass flow through the engine. A reduced mass flow may again force the engine to leave its designated operation point due to being throttled. Numerical causes may also have an impact on the deviation. As presented, a mixing plane approach is chosen to model frame changes. Circumferentially averaging may result in a small distortion of values. This may be stressed by the non-overlapping sections at single passage simulation.

Experimental and numerical mass flows diverge at higher rotation speeds, reaching a maximum discrepancy at 0.075 kg/s at OP5. Speaking in relative terms, experimental data differ from numerical data by −8%. Relative discrepancy increases with higher rotation speeds above 10,000 rpm.

Next, static pressure results for the inlet station are analyzed in more detail. These are illustrated in Fig. 13, featuring plotted lines for both experimental and numerical data. Again, both lines show an equal behavior, with only little discrepancies, as the numerical results are marginally lower than their experimental counterparts are. This effect is more distinct at higher rotation speeds. However, this effect is also in good agreement with our previous findings. We agreed the fact, that our numerical simulation provides a slightly higher mass flow, which results in a higher flow velocity at the outlet station. According to Bernoulli's law for incompressible flows, a higher velocity coerces the static pressure to drop. Consequently, lower static inlet pressures in numerical simulation are a direct result of a higher mass flow rate.
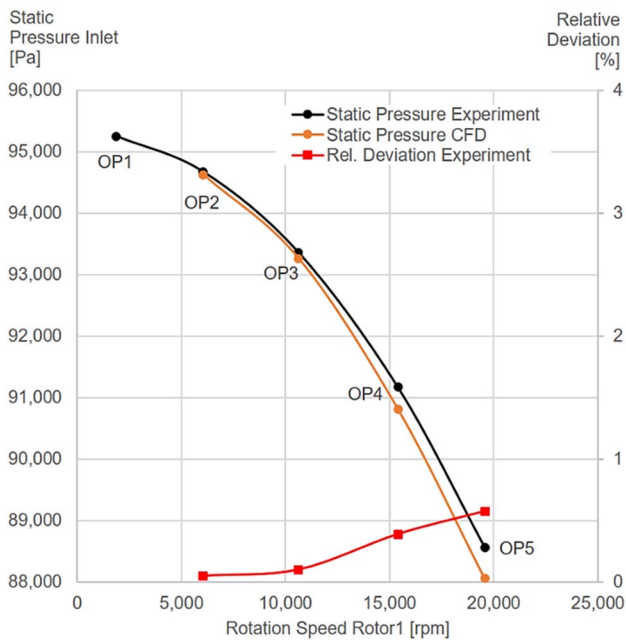
Static Pressure Inlet [Pa] / Relative Deviation [%]



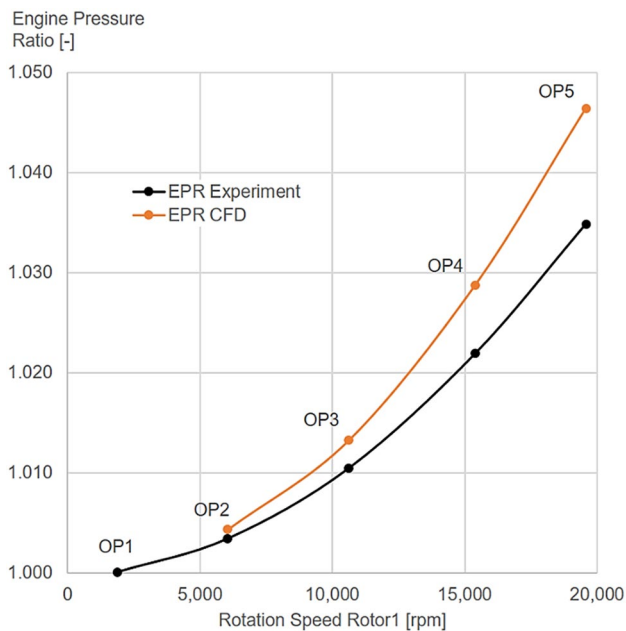**Fig. 13** Comparison of engine inlet static pressure between experiment and CFD simulation



**Fig. 14** Comparison of Engine Pressure Ratio (EPR) between experiment and CFD simulation

Finally, Fig. 14 shows the engine pressure ratio (EPR), calculated between outlet and inlet station's total pressure. Again, these plotted lines deviate to certain extent, just like the mass flow in Fig. 12. EPR results from experiments are lower than numerical results in all operation

points. This may be explained by a higher level of losses, resulting in a smaller total pressure rise throughout the engine.

In summary, the established numerical model seems to be capable to reproduce the most relevant physical effects in a reliable manner. Especially at low rotation speeds, experimental and numerical data agree very well.

## 5 Summary and outlook

The presented study features experimental and numerical investigations of an all-electric, ducted and contra-rotating fan engine. The engine was successfully taken into operation and various operation points have been tested. A general understanding of the engine behavior has been achieved. Experiments show that the engine runs very smooth, with only little vibration, among all considered operation conditions. However, the brushless motors tend to heat up rapidly. This problem shall be addressed in future investigations by developing innovative cooling concepts. Due to heating issues, this study was limited to operation conditions below 80% of maximum design speed. A customized and optimized measurement system was developed, calibrated and tested, in parallel. This system is customized for the tested engine and is found to be accurate and reliable. Thrust, mass flow and pressure values were measured. By these parameters, the engine was found to meet our basic expectations, in terms of behavior. Experiments are accompanied by numerical simulations. Experimental results, such as rotation speeds and pressure values, are taken as input parameters and boundary conditions to initialize these simulations for all operation conditions considered. Simulated and experimentally measured values show a good qualitative agreement, although they slightly differ, especially for higher rotation speeds.

# References

1. Polaczyk, N., Trombino, E., Wei, P., Mitici, M.: A review of current technology and research in urban on-demand air mobility applications. In: vertical flight society autonomous VTOL technical meeting and electric VTOL symposium, Mesa, Arizona (2019)

2. European Commission: Flightpath 2050 – Europe's Vision for Aviation, Report (2011)

3. Deutsches Zentrum für Luft- und Raumfahrt (DLR): Zero emission aviation – Emissionsfreie Luftfahrt, white paper (2020)

4. Aigner, B., Nollmann, M., Stumpf, E.: Design of a hybrid electric propulsion system within a preliminary aircraft design software environment. In: Deutscher Luft- und Raumfahrtkongress, Friedrichshafen (2018)

5. Bowman, C., Felder, J.: Turbo- and hybrid-electrified aircraft propulsion concepts for commercial transport. In: AIAA propulsion and energy forum, Cincinnati, Ohio (2018)

6. Brelje, B., Martins, J.: Electric, hybrid, and turboelectric fixed-wing aircraft: a review of concepts, models, and design approaches. Prog Aerospace Sci. **104** (2019)

7. Cao, W., Mecrow, B., Atkinson, G., Bennett, J., Atkinson, D.: Overview of Electric Motor Technologies used for More Electric Aircraft. IEEE Transactions on Industrial Electronics, **59**(9) (2012)

8. Schimming, P.: Counter-Rotating Fans – An Aircraft Propulsion for the Future. J. Thermal Sci. **12**(2), (2003).

9. Nouri, H., Ravelet, F., Bakir, F., Sarraf, C., Rey, R.: Design and Experimental Validation of a Ducted Counter-rotating Axial-flow Fans System. ASME J. Fluids Eng. **134**(10), (2012)

10. Wang, J., Ravelet, F., Bakir F.: Experimental comparison between a counter-rotating axial-flow fan and a conventional rotor-stator stage. In: 10th European Turbomachinery Conference, Lappeenranta (2013)

11. European Commission: Innovative counter rotating fan system for high bypass ratio aircraft engine – Final Report Summary COBRA (2018)

12. Pundhir, D.S., Sharma, P.B.: A study of Aerodynamic Performance of a Contra-Rotating Axial Compressor Stage. Defence Sci. J. (**42**)3, (1992)

13. Sharma, P.B., Jain, Y.P., Pundhir, D.S.: A Study of some factors affecting the performance of a contra-rotating axial compressor stage. Proceedings of the Institution of Mechanical Engineers, Part A: Power and Process Engineering. (**202**)1, (1988)

14. Ebus, T., Dietz, M.: Small electrically powered contra-rotating turbo fan engines for high-speed aircraft application. *AIAA 2020 Scitech 2020 Forum*, Orlando, Florida (2020)

15. DIN EN ISO 5801: Ventilatoren – Leistungsmessung auf genormten Prüfständen; Deutsche Fassung (2014)

16. ANSYS Inc.: Introduction to CFX – Chapter 12 – Moving Zones, Tutorials (2009)